Research Article | Vol. 13, No. 7 / 1 Jul 2023 / Optical Materials Express 2020
Optical Materials EXPRESS

Dielectric function and band gap determination of single crystal $CuFeS_2$ using FTIR-VIS-UV spectroscopic ellipsometry

NATHAN HALE,[1,*] MATTHIAS HARTL,[2] JOSEF HUMLÍČEK,[3] CHRISTOPH BRÜNE,[2] AND MORTEN KILDEMO[1]

[1]Department of Physics, Norwegian University of Science and Technology (NTNU), NO-7491, Norway
[2]Center for Quantum Spintronics, Department of Physics, NTNU Norwegian University of Science and Technology, NO-7491 Trondheim, Norway
[3]Department of Condensed Matter Physics, Masaryk University, and Central European Institute of Technology, Brno University of Technology, Kotlářská 2, 611 37 Brno, Czech Republic
*nathan.hale@ntnu.no

Abstract: Spectroscopic ellipsometry measurements were performed on antiferromagnetic semiconductor $CuFeS_2$ grown via molecular beam epitaxy. UV/Visible and IR ellipsometry data was merged and modeled to derive the dielectric function of $CuFeS_2$ from 30 meV to 4.5 eV. The $CuFeS_2$ samples were characterized by X-ray diffraction (XRD), atomic force microscopy (AFM) and cross-section scanning electron microscopy (SEM) which gave the crystal quality, surface roughness and sample film thickness. A critical point analysis revealed a direct band gap of 0.76 eV, while modeling gives a carrier concentration of $8 \pm 2 \times 10^{19} \sim cm^{-3}$ and an estimate of the indirect band gap of 0.5 eV. Optically active infrared phonons were observed at 319 cm^{-1} and 350 cm^{-1} with significant Raman active modes at 85.8 cm^{-1}, 265 cm^{-1}, 288 cm^{-1}, 318 cm^{-1} and 377 cm^{-1}. The fitted optical constants were then used to characterize the crystal quality and spatial uniformity.

1. Introduction

Antiferromagnetic (AF) materials have long been studied and investigated but have often been categorized as "Interesting and useless" (Nobel prize lecture Neel). In recent years, however, this assessment has changed, mainly due to advancements in the field of spintronics [1]. Antiferromagnets, with their high frequency dynamics, absence of magnetic stray fields and thereby higher potential storage densities, have generated renewed interest in the field of AF spintronics [2,3].

The AF resonances supported by these materials occur at THz energies and have been experimentally investigated by means of neutron scattering on MnF_2 [4] and attenuated total reflection measurements on FeF_2 [5]. $CuFeS_2$, often referred to as chalcopyrite, was the first semiconductor predicted to have AF properties [6]. In order to explore the AF properties in e.g. spintronics, the supported magnon modes must be carefully described [7], which requires the establishment of optical methods for characterization, monitoring, and control of the growth of the AF semiconductor thin films.

$CuFeS_2$ is the most abundant material found in copper ore [8]. It is a 3-phase semiconductor with a crystal structure related to more common zincblende materials [9]. Single crystal $CuFeS_2$ is of particular interest because of its extremely high Néel temperature = 823 ° K, making it antiferromagnetic at room temperature [10] and well beyond. $CuFeS_2$ crystallizes in the tetragonal chalcopyrite structure ($I\bar{4}2d$ (space group 122)) with a lattice constant of a = 5.289 Å, and c = 10.423 Å. This is a close match to the lattice constant of Si, which is a = 5.431 Å. This combination of high Neel temperature and close lattice match to Si makes $CuFeS_2$ a very

#493426 https://doi.org/10.1364/OME.493426
Journal © 2023 Received 17 Apr 2023; revised 30 May 2023; accepted 1 Jun 2023; published 21 Jun 2023

Optical Materials EXPRESS

interesting candidate for further investigations. Additionally, it is predicted that $CuFeS_2$ is a good candidate for several spin-based effects [11,12], making it a promising material for applications in spintronics [1]. Despite this predicted behavior, the semiconducting and magnetic properties of $CuFeS_2$ remain poorly explored. This is especially true for the behavior of highly crystalline thin films, which are fundamental for semiconducting and spintronics applications.

Previous studies on $CuFeS_2$ have primarily focused on its electronic [9,13] and thermoelectric properties [14]. Other works have demonstrated applications of $CuFeS_2$ in the fields of quantum dots [15], solar cells [16] and energy storage [17]. The vibrational modes of $CuFeS_2$ have also been investigated by means of IR absorption, Raman scattering and inelastic neutron-scattering [18,19].

In terms of optical properties, absorption and reflection measurements have been performed on $CuFeS_2$ in the near-infrared-visible-ultraviolet (NIR-VIS-UV) [20]. There is persistent uncertainty, however, with regards to the band gap properties of $CuFeS_2$. While reflection and absorption measurements have estimated the minimum band gap of $CuFeS_2$ at 0.5 eV [21] and 0.575 eV [22], respectively (both presumably the indirect band gap), density functional theory (DFT) calculations have estimated a direct band gap as high as 0.915 eV [11]. Moreover, thermal methods have predicted an indirect gap as low as 0.3 eV [23].

In this work, we recognize that the low direct band gap of CFS imposes the use of both spectroscopic Fourier transform infra-red (FTIR) ellipsometry and NIR-VIS-UV spectroscopic ellipsometry (SE) in order to accurately extract the dielectric function and thus the related interband and intraband transitions from a thin film. Despite advances in the fitting software for ellipsometry modeling, there seems to have been limited recent research on the optical properties of $CuFeS_2$. Modern ellipsometry techniques have been used on $CuFeS_2$, but only in the context of evaporated nanoparticles [24]. Moreover, $CuFeS_2$ films grown by molecular beam epitaxy (MBE) offer higher crystallinity than samples cut from crystals of variable quality or films grown with the Bridgman method [25]. Here, the focus is placed back on the thin film optical properties of high crystalline $CuFeS_2$, employing these more modern and precise techniques. With remaining uncertainties in material properties such as the direct band gap, carrier concentration and vibrational modes, this work aims to more fully characterize $CuFeS_2$ in the IR-VIS-UV by means of ellipsometry in addition to micro-Raman measurements. By more accurately describing these properties, it is projected that future work can more accurately both simulate and measure the antiferromagnetic and thermoelectric behavior of $CuFeS_2$.

2. Experiment

2.1. Fabrication, imaging and XRD

For this work, single crystalline $CuFeS_2$ thin films were fabricated via molecular beam epitaxy, resulting in films of high crystallinity. Films were grown on 2 inch, single side polished Si(001) wafers of thickness 275 µm, see Fig. 1(a), with a carrier concentration of $10^{15} cm^{-3}$. The $CuFeS_2$ thin films were grown along the [001] direction with their c-axis normal to the substrate. The thicknesses span the range between 30 nm and 150 nm. The details of the MBE growth procedure and further structural analysis will be published elsewhere [26]. Atomic Force Microscopy (AFM) measurements demonstrated the $CuFeS_2$ samples had a surface roughness between 4 nm and 12 nm. To supplement the AFM image, a scanning electron microscopy (SEM) image of the $CuFeS_2$ surface was taken over a larger range with 25k × magnification, as seen in Fig. 1(c). The rectangular features seen in both the AFM and SEM images are islands, a result of a mixed layer and island growth mode (Stranski–Krastanov growth [27]). These islands are likely caused by a mixture of imperfect growth conditions and a moderate lattice mismatch between the Si substrate and the $CuFeS_2$ film of about 2.6%. This mismatch also caused a strain in the sample of approximately 0.8%. The crystallinity of the $CuFeS_2$ samples was determined via the FWHM

Optical Materials EXPRESS

of X-Ray Diffraction (XRD) rocking curves of the (004) reflection peak, as seen in Fig. 1(d) and the aforementioned publication [26].

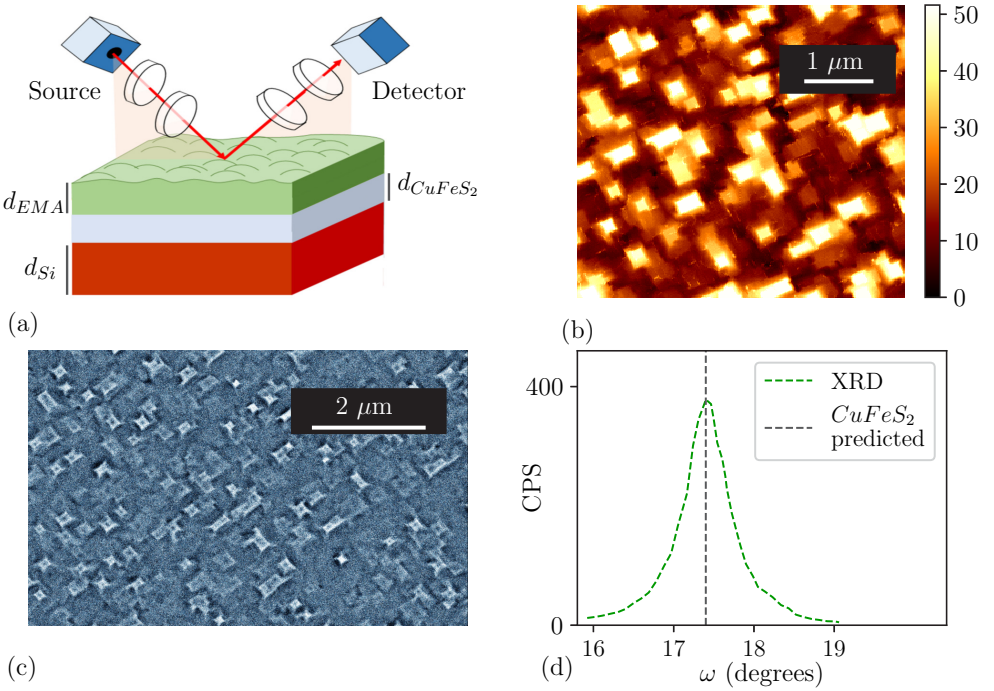

Fig. 1. (a) A schematic of the thin film stack measured by NIR-VIS-UV ellipsometry measurements. (b) AFM image taken over a 5 × 5 μm range showing a 1 μm rule for scale. The color map represents the height of the surface from 0 nm to 41 nm. (c) SEM image of the $CuFeS_2$ surface with a 2 μm rule depicting the scale taken with 25k times magnification.(d) An XRD rocking curve indicating the high crystal quality [26]. The angle for a perfectly crystalline $CuFeS_2$ sample is shown as a black dashed line.

In addition to the SEM images taken to characterize the $CuFeS_2$ surface, as mentioned above, cross-section measurements were also taken to determine the film thickness. To achieve this, the sample was cleaved into a small piece measuring approximately 1 cm × 1 cm. The sample was clamped into the SEM sample holder with the $CuFeS_2$ surface directed perpendicular to the electron beam direction. The sample holder was then tilted by 1 ° such that the $CuFeS_2$ surface could be seen. To resolve the $CuFeS_2$ thickness, a magnification of 100k × was used with a voltage of 10 kV. The secondary electron detector was chosen because it can focus on higher-resolution features.

2.2. IR and NIR-VIS-UV spectroscopic ellipsometry

Spectroscopic ellipsometry in the range (0.7 eV −5.9 eV) was performed on all $CuFeS_2$ thin film samples on c-Si manufactured by MBE using a dual rotating compensator SE, RC2 (JA Wollam company). All measurements were recorded between 1 and 5 days after the samples were fabricated. The experimental data supplied by the system are the ellipsometric angles Ψ and Δ, which are functions of the amplitude and phase of the ratio of r_p and r_s as

$$\rho = \frac{r_p}{r_s} = \tan(\Psi)\exp(i\Delta), \tag{1}$$

Optical Materials EXPRESS

where r_p and r_s are the complex Fresnel reflection amplitudes. Furthermore, the ellipsometric quantities (N = cos(2Ψ), C = sin(2Ψ) cos(Δ), S = sin(2Ψ) sin(Δ)) are also usually considered as measured parameters, and are useful in the fitting procedure.

The off-diagonal elements in the Mueller matrix additionally supplied by the RC2 system are considered to be negligible for the current analysis (see Fig. S1 in Supplement 1). Hence, no significant in plane anisotropy is present, and (Ψ, Δ) or (N, C, S) are sufficient to model the system. Finally, for a uniaxial film with the c-axis perpendicular to the sample surface, it is commonly accepted that ellipsometry is mainly sensitive to the in-plane component of the dielectric function. The pseudodielectric function converges in the limit of no overlayer and a semi-infinite substrate to the bulk dielectric function [28], and is here an efficient way to quickly approximate the dielectric function of the CFS layer by a simple transformation of the measured ellipsometric angles Ψ and Δ

$$\langle\tilde{\epsilon}\rangle = \sin(\theta_i)^2(1 + \tan(\theta_i)^2(\frac{1-\rho}{1+\rho})^2), \tag{2}$$

where θ_i is the angle of incidence and ρ is defined in Eq. (1).

The narrow direct band gap nature of $CuFeS_2$ requires FTIR ellipsometry in order to fully characterize the inter-band behavior. These lower energy measurements also reveal the free carrier and vibrational properties of the material. FTIR ellipsometry measurements were performed on the samples using a variable angle spectroscopic FTIR-ellipsometer (single rotating compensator, IR-VASE, JA Woolam company) in the spectral range 29 meV – 729 meV (234 cm^{-1} – 5879 cm^{-1}) , approximately one month after fabrication. The FTIR-ellipsometer is specified to operate accurately between 333 cm^{-1} to 5900 cm^{-1}. In this work however, data is presented as low as 234 cm^{-1}, as the $CuFeS_2$ samples were sufficiently reflective to produce usable data. Ellipsometric angles Ψ and Δ (or N,C,S) were measured such that the data was consistent with the NIR-VIS-UV data and overlapped. The instrument was set with a resolution of 4 cm^{-1} and an accumulation time of 12 hours. The data was recorded in both spectral regions at 60 °, 65 ° and 70 ° angles of incidence. These angles were chosen to increase the reliability of the results and attempt to produce data near the Brewster angle, where ellipsometry is the most sensitive [29]. The samples were measured in the center of the wafer, such that edge effects could be neglected. A collimated, 3 mm diameter beam was sufficiently large such that any local surface features such as the aforementioned islands were averaged out.

The parameters describing the layer were obtained through nonlinear regression based on the minimization of the mean square error (MSE) between the measured ellipsometric data and the data generated by the model [30]

$$MSE = \frac{1}{n-m-1}\sum_{i=1}^{n}\left(\frac{X_{exp} - X_{calc}}{\sigma_X}\right)^2, \tag{3}$$

where n represents the number of measured data points, m the number of fitting parameters, X the ellipsometric quantity to be measured or calculated, and σ_X is the error in the value. Although N, C, and S are not independent, minimizing the sum of squares of Eq. (3) provides a plausible comparison of the model and measured data.

2.3. MicroRaman system

To further investigate the vibrational modes supported by $CuFeS_2$, MicroRaman measurements were performed using a Renishaw inVia system with a 5 mW, 633 nm source and a 50 x objective. An edge filter was used, which suppressed any Rayleigh scattering present below 80 cm^{-1}. Light was accumulated until no changes in the Ramanshift were observed. Although the Raman system is principally set up for a normal incidence reflection geometry, the high objective is commonly accepted to result in a collection of modes not allowed in the simple geometry.

Optical Materials EXPRESS

3. Results

In order to extract the direct band gap, carrier concentration and dielectric function of the $CuFeS_2$ samples, an optical model was needed to describe the layered system. This modeling was performed using the CompleEASE software (JA Woolam Company). To clarify this complex model, the surface/oxide layer, electrical properties around the direct band gap and lower energy features will be described in different sections.

3.1. Surface roughness/oxides and cross-section

As seen in Fig. 1(b) and (c), the thin film surface is not flat and should accordingly be modeled appropriately. To account for these islands, a more complex EMA was used, as illustrated in the top layer in Fig. 1(a). This EMA layer consisted of $CuFeS_2$, void and an oxide layer. This oxide layer itself was a Bruggeman EMA [31] of both CuO [32] and Fe_2O_3 [33]. Other oxide components were considered, but no better fit was found.

The root-mean-square surface roughness was measured (using the software package Gwyddion) and found to be 6 nm and 8 nm for the two samples. The uncertainty was estimated at ± 2 nm to account for variations in the surface. The $CuFeS_2$ film thicknesses were determined from the SEM images as follows: A color map was chosen that was sensitive to the intensity changes across the cross section of the image. Multiple cross sections were then measured by eye as seen in Fig. 2, the mean values were then calculated as seen in Table 1 and used as starting values for the model. The approximate uncertainties in these mean values were used as upper and lower bounds for the fitted film thicknesses.

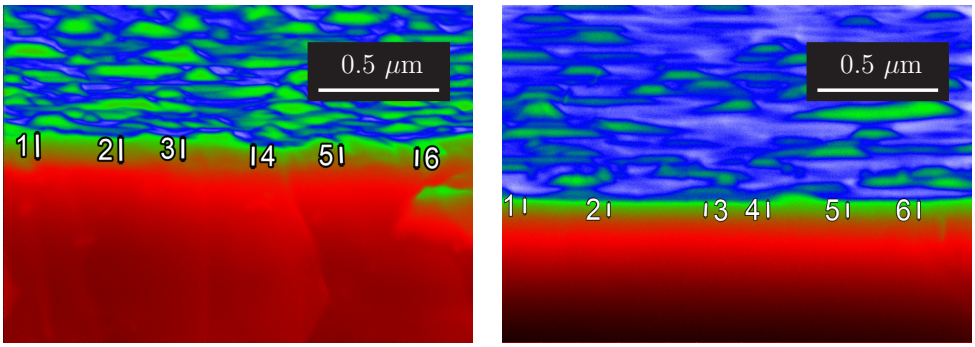

(a) (b)

Fig. 2. The SEM cross-section images for samples (a) CFS-113 and (b) CFS-112. A colormap has been used that is sensitive to the scattering intensity that occurs at the cross section.

Table 1. The individual cross-section measurements on the two $CuFeS_2$ samples, their respective mean values and their surface roughness measurements as found via AFM.

Sample Name	M1 (nm)	M2 (nm)	M3 (nm)	M4 (nm)	M5 (nm)	M6 (nm)	Mean (nm)	AFM (nm)
CFS-113	69	64	59	57	54	56	60	6
CFS-112	91	89	78	77	67	68	78	9

3.2. Ellipsometric results

Figure 3 depicts the combined NIR-VIS-UV and IR ellipsometry angles for two similar but different $CuFeS_2$ samples labeled CFS-112 and CFS-113. Figure 3(a) and (c) show no visible

Optical Materials EXPRESS

mismatch in Ψ for CFS-113 as seen in (a) or Δ in (c). The fact that there is no mismatch in Fig. 3(a) shows the material was homogeneous and that no further oxidation occurred after the NIR-VIS-UV measurements were performed. This implies that all oxidation must have occurred within the first day of growth. The reason for a visible mismatch for CFS-112, seen in Fig. 3(b) is then likely due to the sample being inhomogeneous, as both samples were grown and measured at approximately the same time. This is also consistent with the AFM results, which determined sample CFS-112 to have a higher surface roughness. Figure 3(a) and (b) also show optically active phonons in the infrared. This is seen as two peaks arising above the noise. This more chaotic data is due to the Fabry-Perot resonances of the Si wafer (as the wavelength becomes longer on the order of the film) as well as the absorption due to water vapor in atmosphere (as the FTIR ellipsometry was not in vacuum).

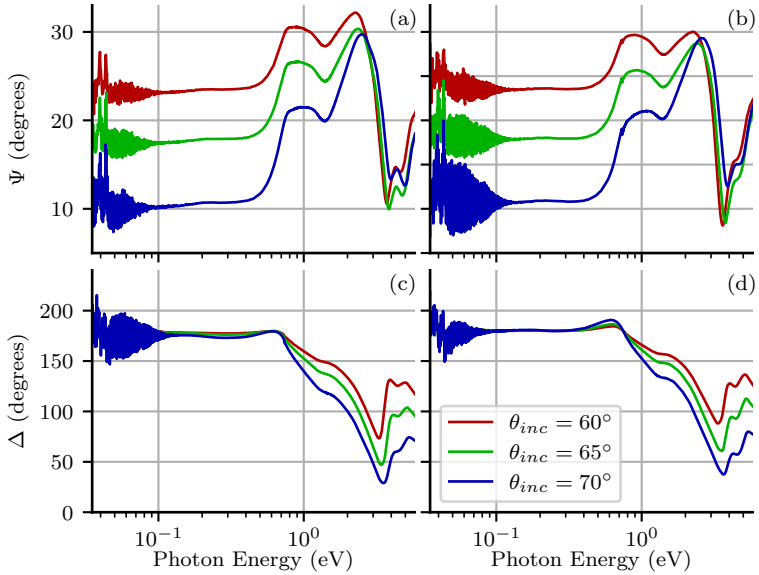

Fig. 3. NIR-VIS-UV and IR ellipsometry data plotted from 0.03 eV to 5.8 eV on a logarithmic scale. A slightly thinner $CuFeS_2$ sample of high crystallinity is presented in (a) and (c) (CFS-113) while data from a slightly less crystalline sample can be seen in (b) and (d) (CFS-112).

To gain a quick insight into the optical response of the material, the pseudodielectric function was plotted in Fig. 4 for both samples, CFS-112 and CFS-113. Although the pseudodielectric function is an approximation as it assumes a bulk layer with no EMA layer, it can give information regarding the position of optical features. For example, the plot shows a prominent peak in Re($<\tilde{\epsilon}>$) at approximately 0.75 eV with a corresponding sharp increase in Im($<\tilde{\epsilon}>$). This could indicate the presence of a critical point. To a lesser extent, a similar argument could be made for a weaker peak at 1.6 eV.

To make a more refined model, the top EMA layer and Si substrate were included. The Si layer was modeled as semi-infinite with its optical properties taken from literature [33]. The $CuFeS_2$ layer and EMA surface layer thicknesses were set as fitting parameters, with their sum equaling the measured cross-sections as seen in Table 1. To model the dielectric function of the $CuFeS_2$ layer, a B-spline was used. This method uses a set of basis-spline functions and nodes with a set resolution to fit the ellipsometric data. To increase the speed and probability of a good fit, initial optical constants were used based on $CuFeS_2$ from the literature [21]. This B-spline fit is shown in Fig. 5(a) and bears some resemblance to the pseudodielectric plot in Fig. 4, which has a strong

Optical Materials EXPRESS

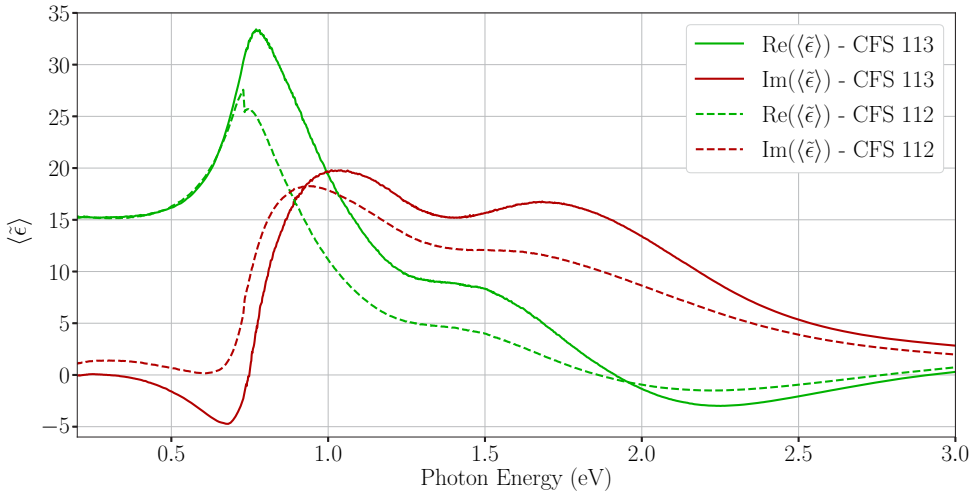

Fig. 4. Real and imaginary components of the pseudodielectric function of $CuFeS_2$ samples with an angle of incidence of 70°. Samples CFS-113 and CFS-112 are distinguished by full-lined and dashed curves, respectively.

Table 2. The oscillator number (with relation to Fig. 5), oscillator type and oscillator parameters including amplitude broadening, position, peak energy, bandgap, resistivity and carrier lifetime. Due to the large span in energy, values are given in both cm^{-1} and eV. The thickness of the CFS-113 sample was fitted to 46 ± 1 nm, with the corresponding EMA/roughness layer height being 7 ± 2 nm. For definitions of terms and context within equations, please see the supporting information document.

Osc number	Osc type	Amp2	Br3 (cm^{-1}/eV)	Eo1 (cm^{-1}/eV)	Eg1 (cm^{-1}/eV)	Ep1 (cm^{-1}/eV)	N (cm^{-3})	μ ($cm^2V^{-1}s^{-1}$)
1	Cody-Lorentz	3.810	1121/0.139	6235/0.773	3920/0.486	4130/0.512	-	-
2	Cody-Lorentz	8.124	6049/0.750	8727/1.082	6138/0.761	588/0.0705	-	-
3	Tauc-Lorentz	23.911	5864/0.727	15704/1.947	-	-	-	
4	Drude	-	-	-	-	-	8.0×10^{19}	1.39
5	Gaussian	5.27	14881/1.845	48208/5.977	-	-	-	-
6	Gaussian	2.88	9437/1.17	34230/4.244	-	-	-	-
7	Lorentz	91.767	8.70/0.001079	319/0.0395	-	-	-	-
8	Lorentz	100.069	6.24/0.000774	350/0.0434	-	-	-	-

absorption edge at around 0.75 eV as well as a peak at around 1.7 eV. Note that the B-spline model was fitted from 50 meV, excluding the IR active phonons seen in Fig. 3(a) and (b), as it ignores the noisier, low energy data (more appropriately modeled by dispersion models) while supplying high resolution in the band gap region. This model is Kramer's Kronig consistent, meaning the real component can be computed from the imaginary, using the relation [34].

$$\epsilon_1(E) = 1 + \frac{2}{\pi}\int_0^{+\infty} \frac{\epsilon_2(E')E' - \epsilon_2(E)E}{E'^2 - E^2} dE', \tag{4}$$

where E' is the energy variable to be integrated and ϵ_1 and ϵ_2 are the real and imaginary components of the dielectric function respectively. The B-spline model is therefore more physically meaningful, having only positive Im($\tilde{\epsilon}$) and a signature of a free carrier contribution at low energies.

To gain more physical meaning from this B-spline fit, the optical constants were parameterized by a generic oscillator model. The equations used in this method are taken from the literature

Optical Materials EXPRESS

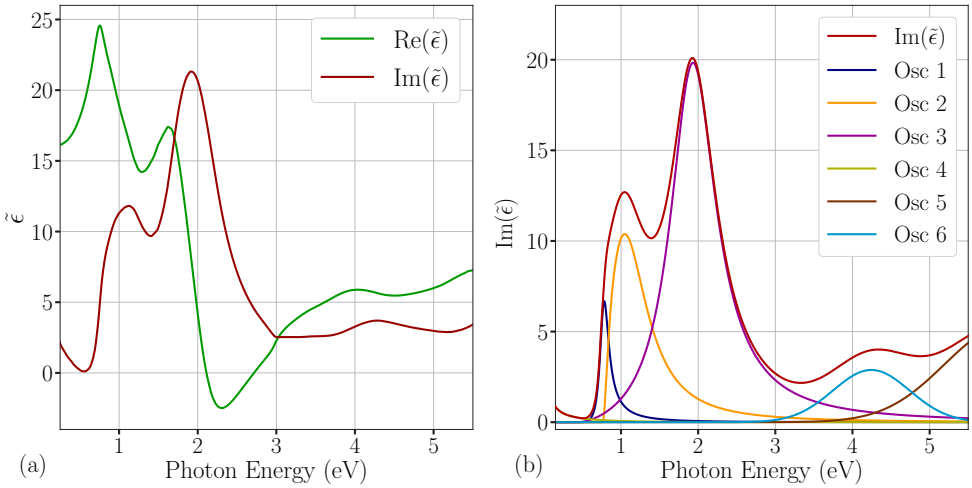

Fig. 5. (a) The real and imaginary components of the dielectric function for $CuFeS_2$ derived from the B-spline fit. (b) The imaginary component of the dielectric function of $CuFeS_2$ after the B-spline fit was parameterized with a generic oscillator model. The individual oscillators listed here from 1– 6 are described in Table 2

[35] and shown in the SI. In order to characterize the band gap region, Cody-Lorentz oscillators were used [36]. Above this immediate band gap region, Tauc-Lorentz oscillators were used to model the charge transfer peaks. This was chosen as these oscillators have no contributions below the indirect band gap [37,38].

The absorption peaks at higher energies are said to originate from charge transfer from the valence band to the d-orbitals of Fe atoms [21] and have been modeled with Gaussian peaks to reflect the multiple possible transitions they represent. The energy range of the generic oscillator model was expanded from the B-spline fit to include the IR active phonon peaks below 50 meV. Arising from a single mechanism, these observed phonon peaks were modeled with Lorentzian oscillators. To model the increased absorption at lower energies caused by free carriers, a Drude model was incorporated. The critical point-like feature seen in both the pseudodielectric function and B-spline fits of ≈ 0.75 eV was used as an initial guess for the direct band gap.

In order not to overfit the model, some model parameters were set. For example, in the Drude model, DFT calculations have determined the effective mass of $CuFeS_2$ electrons with $m* = 0.81 m_0$ [11], where m_0 is the free electron mass. With this value set, the Drude model fits the carrier concentration N and electron mobility μ as seen in Table 2

The Cody-Lorentz peaks [36] in Table 2 show a strong peak centered at 1.082 eV with a Cody gap at 0.76 eV, and a weaker, broader peak centered at 0.773 eV, with a Cody gap at 0.486 eV. The two Cody gaps were purposely not fixed in order to model the complex nature of the 2D critical point and the indirect band gap, as discussed further in the analysis below. The Tauc-Lorentz peak [37] is significant, being centered on 1.947 eV. The Drude model gave a carrier concentration of 7.9×10^{19}. This is higher than previously computed with optical modeling [21] but approximately consistent with values from charge and spin transport measurements [39,40]. The electron mobility was fitted at 1.39 $cm^2V^{-1}s^{-1}$ which is consistent with the range of values previously found [39]. The fitted Gaussian oscillators are relatively broad and occur at 5.98 eV and 4.24 eV.

Optical Materials EXPRESS

3.3. Lattice resonances from FTIR ellipsometry and Raman spectroscopy

The two Lorentzian peaks listed in Table 2 correspond to the IR-active phonons seen in the raw ellipsometric data in Fig. 3. The fitted Im($\tilde{\epsilon}$) of these peaks, occurring at 319 cm^{-1} and 350 cm^{-1} (39.5 meV and 43.4 meV) are shown in Fig. 6(a). Note that although there is a clear Drude component representing the contribution from free carrier absorption, it is not strong enough to suppress the phonon resonances.

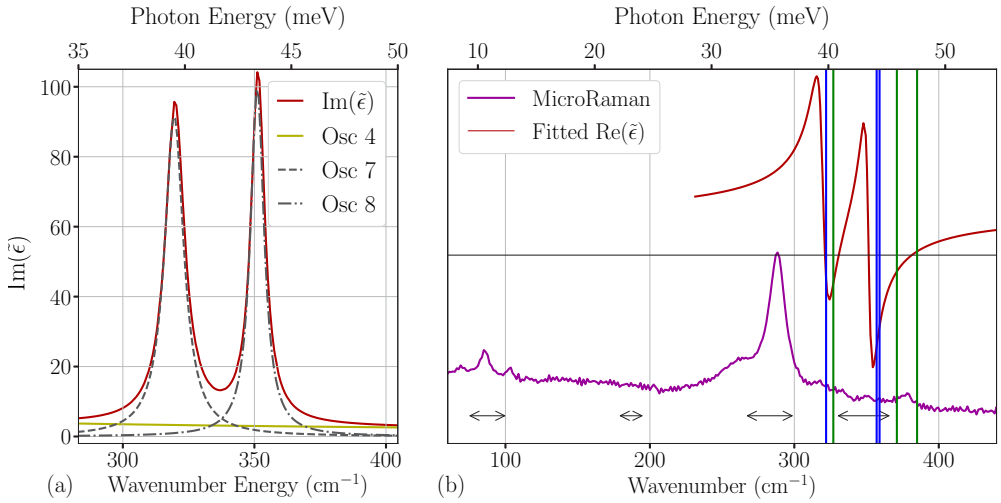

Fig. 6. (a) Fitted Im($\tilde{\epsilon}$) for $CuFeS_2$ in the mid-IR region with three oscillators shown, as described in Table 2. (b) MicroRaman spectra (purple) plotted on a logarithmic scale, indicating photon count number. The black double-sided arrows correspond to regions of calculated phonon resonances at the Γ point [41]. The real part of the fitted dielectric function (red) plotted on a different y-axis from the Raman spectra the blue and green vertical lines display the reported positions of TO and LO modes [18,42].

The IR-active phonons are accompanied by Raman-active modes, which are listed in Table 3 and shown in Fig. 6(b). The horizontal black arrows correspond to vibrational modes at the Γ point as calculated by DFT [41].

Table 3. The five strongest fitted Raman peaks, showing peak positions, peak width, the ratio of Gaussian and Lorentzian components of the convoluted profiles used in the fit and the peak area normalized to the strongest peak at 288 cm^{-3}, for sample CFS-112.

Peak frequency (cm^{-1}/meV)	Frequency width (cm^{-1}/meV)	Gaussian to Lorentzian ratio (%)	Normalized peak area
85.8/10.6	6.60/0.818	0	0.067
265/32.9	38.3/4.75	100	0.22
288/35.7	8.11/1.01	24	1.0
318/39.4	9.34/1.16	100	0.016
377/46.7	11.0/1.36	100	0.016

Optical Materials EXPRESS

4. Discussion

4.1. Direct band gap electronic transitions

The results further discussed in this work focus on sample CFS-113, which is of higher quality. the first peak of the real part, and the step-like increase of the imaginary part of the dielectric function at 0.75 eV (extracted by B-spline - Fig. 5(a)) resemble a strong 2D critical point corresponding to the minimum direct band gap. To further establish this critical point feature, a second derivative of a high resolution fitted B-spline dielectric function (0.02 eV resolution) was calculated using a Savitzky-Golay three polynomial window over 0.1 eV. Figure 7(a) shows the complex second-derivative function, which can be modeled by multiple lineshape functions of the form [35]

$$\tilde{\epsilon}'' = \frac{d^2\tilde{\epsilon}}{dE^2} = -\prod_{j=1, j\neq d/2}^{n} (d/2-j)Ae^{i\varphi}(E - E_0 + i\Gamma)^{\frac{d}{2}-3}, \tag{5}$$

where A is the CP amplitude, d is the dimensionality of the CP, φ is an angle describing the nature of the CP (min, saddle,max, or mixed), E_0 is the CP position and Γ, the broadening. Several dimensions were investigated, but the 2-dim CP solution was preferred, and appears reasonable given the reduced symmetry of the crystal. Similarly, the number of CPs was increased up to a maximum of six (adding further critical points appears difficult to legitimize given the current experimental resolution). Adding these CPs was motivated by the inspection of the dielectric function (maxima and minima) and by the features in its second derivative, but also by recent band structure calculations [11]. The fitted parameters were found to vary somewhat depending on the overlayer (where no overlayer removal consists in fitting the second derivative of the pseudodielectric function), but one set of reasonable parameters is reported in Table SI1, found in the Supplement 1. These parameters can then be used to compute the general form of the dielectric function for each 2D CP following [35]

$$\tilde{\epsilon} = C - Ae^{i\varphi} ln(\hbar\omega - E_0 + i\Gamma), \tag{6}$$

where the dimension has been assumed to be 2D. The four strongest peaks are shown in Fig. 7(b)-(e), where the y axis is on an arbitrary scale and x-axis has been normalised.

The second derivative analysis confirms that there is indeed a very strong and narrow 2D Min CP at 0.76 eV. This is thus an accurate estimate of the minimum direct band gap of highly crystalline $CuFeS_2$.It is recalled that SE is mainly sensitive to the in-plane component of the dielectric function, and it is therefore presumed that the current analysis will only reveal the transitions allowed for $\mathbf{E} \perp \hat{\mathbf{c}}$. In terms of the most recent band structure calculations [11], we assign this CP to the X(VB-1) $\rightarrow$ X(CB-1) = 0.76 $\pm$ 0.005 eV (i.e. 0.168 eV below the value calculated by Brekke et al. [11]), where VB-1 denoted the upper valence band, and CB-1 denoted the lowest conduction band in their calculations. Relatively flat bands are likely an artifact of the CP strengths being proportional to the reduced effective mass [14]. The phase of the VB maxima and CB minima indicates that it is a slightly mixed CP of mainly minimum character. Angle Resolved Photo Emission Spectroscopy (ARPES) can potentially accurately determine these values, but is complicated by both the surface oxides and roughness.

The remaining CPs (weak 0.875 eV min/mixed, weak 1.1 eV saddle, 1.50 eV broad and weak minimum (insignificant), 1.68 eV strong minimum and 2.18 eV significant maximum) appear more difficult to establish with a similar accuracy, and more experimental data is needed to relate it to the electronic band structure, see Supplemental for further discussion. However, the strong maximum near 2.2 eV appears as a typical E_2 CP at Γ.

Adding to the case that sample CFS-113 has superior optical properties compared with CFS-112, are the differing CP model parameters, as listed in the Supplement 1 (Table S3).

Optical Materials EXPRESS

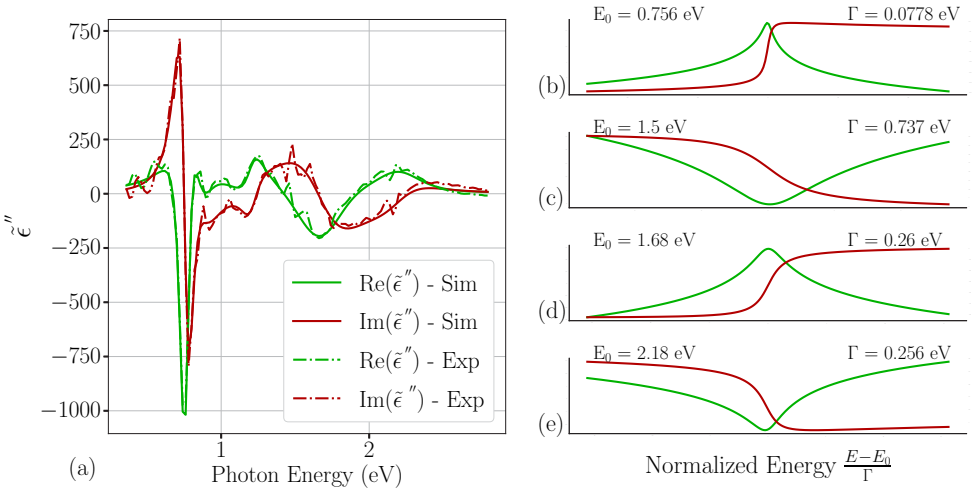

Fig. 7. (a) Real and imaginary components of the 2nd derivative of the fitted B-spline model for sample CFS - 113. The simulated and experimental values are distinguished by lined and dash-dotted lines respectively. (b)-(e) The dielectric function of each distinct spectral structure in (a).

4.2. Indirect band gap

The minimum of the imaginary part of the dielectric function at 0.54 eV is speculated to be close to the indirect band gap; similarly, the Cody-Lorentz oscillator model gives a lowest Cody gap (interpreted as a possible indirect band gap) of around 0.485 eV. While some DFT calculations have placed the indirect gap from X(VB-1) → Z(CB-1) at 0.35 eV [14], more modern works [11] report the gap from X(VB-1) → N(CB-1) at 0.532 eV (when scissor corrected in this work by 0.168 eV). This is reasonable in accordance with our findings and well within the error of our determination of the indirect band gap via SE.

4.3. Parametric dispersion model of the dielectric function

The parametric model was based on a large number of oscillators. It is noted that modeling the dielectric function based on 2D CPs is known to be difficult [35]. A more pragmatic complete working model allows for the determination of the phonon polaritons as seen in Fig. 8(a), the free carrier response, and supplied a good estimate of the critical points (Table SI1). In fact, the center of the Cody-Lorentz oscillators is believed to emulate the 2D direct CPs as their center energies (0.77 eV and 1.08 eV) are in reasonable correspondence to the CP energies of the 2nd derivative analysis. Replacing the Cody Lorentz oscillators with Tauc Lorentz oscillators gave a considerably worse fit. The Cody gap of the lower Cody-Lorentz oscillator gives a lower estimate of the indirect band gap (0.48 eV). Recent band calculations of $CuFeS_2$ indicate a range of possible transitions, contributing to absorption above both the direct and indirect band gaps [11]. The higher energy oscillators are the sum of a large number of critical points, which are modeled by a Tauc Lorentz oscillator at 1.9 eV (near the 2D maximum). Finally, two additional Gaussian oscillators at 4.2 eV and 6 eV have been added to the model lineshapes. It is observed that the oscillators at 1.08 eV, at 1.9 eV and the two upper Guassian peaks at 4.2 eV and 6 eV are in good correspondence with the oscillators A, B and C reported by Oguchi et al. [21]. However, we note from Fig. 8(b) that the dielectric functions are surprisingly different. The parametric model revealed that the free carrier density was estimated at $8 \pm 2 \times 10^{19}$ cm^{-3} for sample CFS-113 and $4 \pm 2 \times 10^{20}$ cm^{-3} for sample CFS-112. These are in approximate agreement with recent results

Optical Materials EXPRESS

of Ref. [41]. The critical points were also modified with a small lowering of the direct band gap, and the critical points appeared less intense. However, the surface roughness was higher for CFS-112, which increases the uncertainty, in particular at higher photon energies, where the BEMA overlayer approximation is expected to be worse.

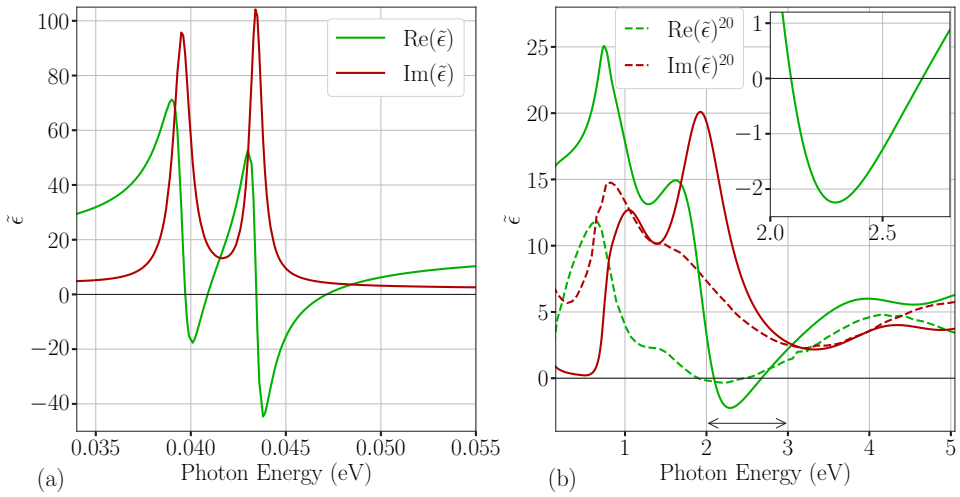

Fig. 8. (a) and (b) the real and imaginary components of the permittivity over the IR and visible frequency ranges, with the real part found via Kramer's Kronig relation. For comparison, (b) includes previously modeled values for the dielectric function. The inset shows a closeup of Re($\tilde{\epsilon}$) in the plasmonic region in the visible.

The full complex dielectric function of $CuFeS_2$, as derived with the parametric model, is shown in Fig. 8. The corresponding complex refractive index can be found in Fig. S1. The region around the IR-active phonons is shown in Fig. 8(a). The two peaks of enhanced absorption are followed by two regions of negative Re($\tilde{\epsilon}$), as expected. This should support two surface modes known as surface phonon polaritons [43]. The large Im($\tilde{\epsilon}$) however, would mean these surface modes are heavily suppressed. The dielectric function extracted using the B-spline and the parametric model were overall found to be similar, with the main difference seen in the contribution from free carriers to the absorption. A further comparison is made in Fig. S4 in the Supplement 1.

Figure 8(b) compares our results with previously performed reflectance measurements [21]. The past work shows similar (but smaller in amplitude) peaks in Re($\tilde{\epsilon}$) occurring at approximately 0.6 eV, 1.5 eV and 4.2 eV. Rather large deviations are likely caused by differences in sample quality as well as the measurement methods, including the treatment of surface layers.

The new fit also shows a small plasmonic region in which Re($\tilde{\epsilon}$) < 0, as seen in the inset of Fig. 8(b). Interestingly, previous work on $CuFeS_2$ quantum dots has attributed a Localized surface Plasmon resonance at approximately 2.5 eV to such a LSPR [44]. For a lossless, spherical particle, such a resonance occurs when Re($\tilde{\epsilon}$) $= -2$ [45], a result that is approximately consistent with the dielectric function seen in the inset; however, the large absorption seen as the large values of Im($\tilde{\epsilon}$) would make the observation of LSPR unlikely with these optical response functions.

The used Si substrates contributed signals from light reflected from the backside. Because the Si wafer was single-sided polished, the backside scatters some of the light. The model used in this work omits the corresponding Fabry-Perot oscillations, as it assumes the substrate to be semi-infinite. This inaccuracy contributes to an increased MSE. An additional source of error comes from the mismatch in resolution between the FTIR and NIR-VIS-UV systems. The two data sets must be stitched together despite the NIR-VIS-UV system having a much higher

Optical Materials EXPRESS

resolution (2.5 nm in the NIR and 1 nm at VIS-UV frequencies). Although the data is then interpolated before fitting, higher-frequency features can only be measured in the NIR-VIS-UV range. To address this in future work, a higher resolution should be used in the 0.3 eV – 1.4 eV range. More details regarding the accuracy of the generic oscillator fit can be found in Section B of the Supplement 1.

4.4. Vibrational modes

The vibrational modes present in $CuFeS_2$ have previously both been calculated via classical spring [18,46] and DFT [41] and experimentally investigated by both neutron scattering and IR reflection and transmission measurements [18,19].

Figure 6(b) shows the recorded micro-Raman spectrum for sample CFS-112, where the horizontal black double-sided arrows correspond to the DFT calculated Raman-active phonon peaks [18]. Furthermore, all peaks are listed in Table 3, with the weakest ones only appearing after a sufficiently long recording time. The dominating Raman peaks that also occur at low accumulation times are at 85 cm^{-1}, a broad shoulder at 265 cm^{-1}, the strongest peak at 288 cm^{-1}, and two weaker peaks at 318 cm^{-1} and 377 cm^{-1}.

Most of modes listed in Table 3 do indeed approximately fall in the regions marked by the horizontal arrows seen in Fig. 6(b). However, the other observed peaks at 318 cm^{-1} and 377 cm^{-1} do not have such a good correspondence. Figure 6(b) also compares our results (for $\mathrm{Re}(\tilde{\epsilon})$) with the $\Gamma_{5L,T}$ and $\Gamma_{4L,T}$ modes identified in Refs. [18,42]. The transverse and longitudinal modes are shown in blue and green, respectively. As the latter results were obtained from a piece of $CuFeS_2$ cut from mineral, differences in crystal qualities could explain the (slight) discrepancy in the mode positions.

4.5. Control and monitor of MBE films

Ellipsometry has previously been used to characterize the homogeneity and quality of thin films [47], with the overall aim of reaching specific targets in the fields of photovoltaics [35], and should thereby also be a good approach for thermoelectric [41] and spintronic materials [7].

4.5.1. Crystal quality

The ellipsometric angles Ψ are qualitatively compared for $CuFeS_2$ samples with varying crystal quality. Figure 9(a) shows Ψ for three samples of varying crystal quality, as verified from XRD measurements seen in Fig. 9(b). The energy range focuses on the phonons in the infrared. The plot shows a decreasing phonon peak prominence for decreasing crystallinity. Although this analysis is just qualitative, FTIR ellipsometry is sufficiently surface sensitive to present itself as an additional method to reveal the $CuFeS_2$ thin film quality.

4.5.2. Spatial uniformity of the film

Moreover, although the beam size of a standard RC2 ellipsometer is on the order of 3 mm × 7 mm, focusing probes can reduce it to typically 100μm. By using a translation stage with movements of order 10s of μm's, sample parameters can be determined as a function of sample position, as illustrated in Fig. 9(c). Here the previously fitted generic oscillator model is used to fit the thickness and surface roughness of sample CFS-113. The direction of the cuts is shown in Fig. 9(c) in relation to the 2-inch wafer (seen in blue). The thickness is approximately equal to the extracted thickness from the generic oscillator plot over the entire wafer. Moreover, the thickness profile shows a minimum thickness in the middle of the sample, with increasing thickness toward the edges. This thickness variation, although small as seen in Fig. 9(d) could possibly be explained by the temperature variations over the sample during growth. The surface roughness is also shown in 9(c), but does not follow the same trend. This could simply be due to

Optical Materials EXPRESS

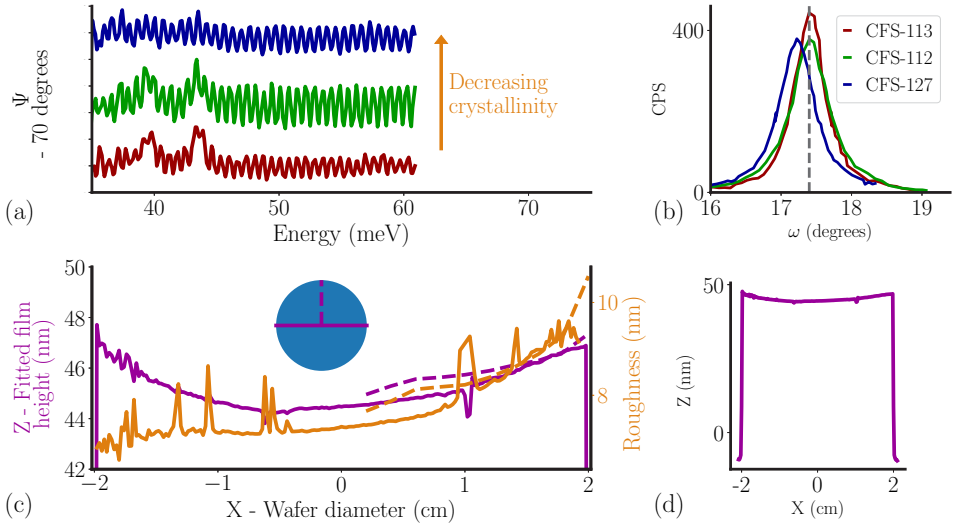

Fig. 9. (a) The ellipsometric angle Ψ showing the phonons energies for three different samples of varying crystallinity. (b) XRD results for three $CuFeS_2$ samples of varying quality. (c) The fitted sample film thickness and surface roughness along different direction across the wafer. (d) A zoomed-out plot of the fitted film thickness.

bending or damage to the sample near one edge and is unlikely to be the result of fabrication. Additionally, the plot shows small scale peaks that most likely correspond to dust particles.

4.5.3. Magnon modes and metrology

No sign of magnon modes was observed by THz SE in the range 0.1 THz – 1.8 THz, although on a film of lower quality than the current films. Having established the characteristics of a high quality semiconductor $CuFeS_2$ layer, it will facilitate further improving the growth process in order to search for layers of sufficient quality (thickness and semiconducting quality) that may reveal a clear magnon resonance. The lower Raman modes most likely correspond to the phonons reported by DFT calculations near the Γ point [18], although the measured modes are in fact at lower wavenumbers than the calculated ones. It is interesting to note that a hypothetical Magnon resonance is speculated to exist in this range. It is envisaged that accurate DFT calculations of the magnon spectrum and the phonon spectrum may resolve this issue.

The optical metrology appears critical to monitor and achieve control over the quality of the layers. It is envisaged that high-quality $CuFeS_2$ layers with strong magnon resonances can be realized through tight control and monitoring of the film quality.

5. Conclusion

In this work, FTIR-VIS-UV ellipsometry was performed on high-crystalline $CuFeS_2$ samples fabricated via MBE. Previously derived optical constants, surface roughness and film thickness were all used to guide a B-spline fit of the ellipsometry data. Both a CP and a parametric dispersion model were used, identifying a direct band gap position of 0.76 eV and an indirect band gap roughly estimated to 0.5 eV. The CP model was based on 2D-CPs and was informed by DFT calculations. The B-spline fit was then parameterized using six generic oscillators, giving physical insights into the material, such as a carrier concentration of $8 \times 10^{19}\ cm^{-3}$ and two IR active phonon peaks occurring at 319 cm^{-1} and 350 cm^{-1} (39.5 meV and 43.4 meV). Multiple vibrational modes were also revealed via MicroRaman, including prominent peaks at 85.8 cm^{-1},

Optical Materials EXPRESS

265 cm^{-1}, 288 cm^{-1}, 318 cm^{-1} and 377 cm^{-1}. Metrological methods were then employed to aid in the high level of control enabled by the MBE fabrication. This included a phonon peak prominence and XRD position correspondence and a minimum in sample thickness occurring in the center of the sample.

Funding. EEA grant (EMP-CZ-MOP-2-013); NTNU Nano Impact Fund.

Acknowledgements. N. Hale acknowledges help from professor Kamil Postava and his group at VŠB-Technical University of Ostrava, Institute of Physics. Acknowledgments are also made to the Materials Optics unit at Linköping University, Sweden, and specifically Prof. Hans Arwin for their help with the FTIR measurements. CzechNanoLab project LM2018110 funded by MEYS CR is gratefully acknowledged for the financial support of the measurements.

Disclosures. The Authors declare no conflict of interests.

Data availability. The data underlying the results presented in this paper are not publicly available at this time but may be obtained from the authors upon reasonable request

Supplemental document. See Supplement 1 for supporting content.

References

1. I. Žutić, J. Fabian, and S. Das Sarma, "Spintronics: fundamentals and applications," Rev. Mod. Phys. **76**(2), 323–410 (2004).
2. T. Jungwirth, X. Marti, P. Wadley, and J. Wunderlich, "Antiferromagnetic spintronics," Nat. Nanotechnol. **11**(3), 231–241 (2016).
3. T. Kosub, M. Kopte, R. Hühne, P. Appel, B. Shields, P. Maletinsky, R. Hübner, M. O. Liedke, J. Fassbender, O. G. Schmidt, and D. Makarov, "Purely antiferromagnetic magnetoelectric random access memory," Nat. Commun. **8**(1), 13985 (2017).
4. B. Lüthi, D. L. Mills, and R. E. Camley, "Surface spin waves in antiferromagnets," Phys. Rev. B **28**(3), 1475–1479 (1983).
5. M. R. F. Jensen, S. A. Feiven, T. J. Parker, and R. E. Camley, "Experimental determination of magnetic polariton dispersion curves in FeF_2," Phys. Rev. B **55**(5), 2745–2748 (1997).
6. K. G. Nikiforov, "Magnetically ordered multinary semiconductors," Prog. Cryst. Growth Charact. Mater. **39**(1-4), 1–104 (1999).
7. N. Hale, I. Simonsen, C. Brüne, and M. Kildemo, "Use of 4×4 transfer matrix method in the study of surface magnon polaritons via simulated attenuated total reflection measurements on the antiferromagnetic semiconductor MnF_2," Phys. Rev. B **105**(10), 104421 (2022).
8. Y. J. Xian, S. M. Wen, J. S. Deng, J. Liu, and Q. Nie, "Leaching chalcopyrite with sodium chlorate in hydrochloric acid solution," Can. Metall. Q. **51**(2), 133–140 (2012).
9. S. Conejeros, P. Alemany, M. Llunell, I. de P. R. Moreira, V. Sanchez, and J. Llanos, "Electronic structure and magnetic properties of $CuFeS_2$," Inorg. Chem. **54**(10), 4840–4849 (2015).
10. V. Baltz, A. Manchon, M. Tsoi, T. Moriyama, T. Ono, and Y. Tserkovnyak, "Antiferromagnetic spintronics," Rev. Mod. Phys. **90**(1), 015005 (2018).
11. B. Brekke, R. Malyshev, I.-H. Svenum, S. M. Selbach, T. Tybell, C. Brüne, and A. Brataas, "Low-energy properties of electrons and holes in $CuFeS_2$," Phys. Rev. B **106**(22), 224421 (2022).
12. A. N. Bogdanov and D. A. Yablonskii, "Contribution to the theory of inhomogeneous states of magnets in the region of magnetic-field-induced phase transitions mixed state of antiferromagnets," Soviet Physics - JETP (English Translation) **69**, 142–146 (1989).
13. J. A. Tossell, D. S. Urch, D. J. Vaughan, and G. Wiech, "The electronic structure of $CuFeS_2$, chalcopyrite, from X-ray emission and X-Ray photoelectron spectroscopy and x calculations," J. Chem. Phys. **77**(1), 77–82 (1982).
14. H. Xie, X. Su, S. Hao, C. Wolverton, C. Uher, X. Tang, and M. G. Kanatzidis, "Quasilinear dispersion in electronic band structure and high seebeck coefficient in $CuFeS_2$-based thermoelectric materials," Phys. Rev. Mater. **4**(2), 025405 (2020).
15. B. Bhattacharyya and A. Pandey, "$CuFeS_2$ quantum dots and highly luminescent $CuFeS_2$ based core/shell structures: Synthesis, tunability, and photophysics," J. Am. Chem. Soc. **138**(32), 10207–10213 (2016).
16. Y. Wu, B. Zhou, C. Yang, S. Liao, W.-H. Zhang, and C. Li, "$CuFeS_2$ colloidal nanocrystals as an efficient electrocatalyst for dye sensitized solar cells," Chem. Commun. **52**(1), 1 (2016).
17. K. Deen and E. Asselin, "On the use of a naturally-sourced $CuFeS_2$ mineral concentrate for energy storage," Electrochim. Acta **297**, 1079–1093 (2019).
18. W. H. Koschel and M. Bettini, "Zone-centered phonons in $AIBIIIS_2$ chalcopyrites," Phys. Status Solidi B **72**(2), 729–737 (1975).
19. M. J. Harris, M. P. Zinkin, and I. P. Swainson, "Phonons and spin waves in the magnetic semiconductor chalcopyrite $CuFeS_2$," Phys. Rev. B **55**(11), 6957–6959 (1997).
20. T. Teranishi, K. Sato, and K. Kondo, "Optical properties of a magnetic semiconductor: Chalcopyrite $CuFeS_2$.: I. absorption spectra of $CuFeS_2$ and fe-doped $CuAlS_2$ and $CuGaS_2$," J. Phys. Soc. Jpn. **36**(6), 1618–1624 (1974).

Optical Materials EXPRESS

21. T. Oguchi, K. Sato, and T. Teranishi, "Optical reflectivity spectrum of a $CuFeS_2$ single crystal," J. Phys. Soc. Jpn. **48**(1), 123–128 (1980).
22. L. Barkat, N. Hamdadou, M. Morsli, A. Khelil, and J. Bernède, "Growth and characterization of $CuFeS_2$ thin films," J. Cryst. Growth **297**(2), 426–431 (2006).
23. Y. Li, T. Zhang, Y. Qin, T. Day, G. Jeffrey Snyder, X. Shi, and L. Chen, "Thermoelectric transport properties of diamond-like $Cu1_xFe_{1+x}S_2$ tetrahedral compounds," J. Appl. Phys. **116**(20), 203705 (2014).
24. E. Bastola, K. Bhandari, I. Subedi, N. Podraza, and R. Ellingson, "Structural, optical, and hole transport properties of earth-abundant chalcopyrite ($CuFeS_2$) nanocrystals," MRS Commun. **8**(3), 970–978 (2018).
25. R. Adams, R. Beaulieu, M. Vassiliadis, and A. Wold, "Crystal growth of $CuFeS_2$," Mater. Res. Bull. **7**(2), 87–91 (1972).
26. M. Hartl, S. brinkman, P. Chatterjee, N. Hale, I. Zelenina, M. Kildemo, M. Nord, and C. Brüne, "Epitaxial growth of chalcopyrite $CuFeS_2$ on Si(001) by MBE," [Unpublished manuscript].
27. J. A. Venables, *Introduction to Surface and Thin Film Processes* (Cambridge University, 2000).
28. D. E. Aspnes and A. A. Studna, "Dielectric functions and optical parameters of Si, Ge, GaP, GaAs, GaSb, InP, InAs, and InSb from 1.5 to 6.0 eV," Phys. Rev. B **27**(2), 985–1009 (1983).
29. H. Butt, K. Graf, and M. Kappl, *Physics and Chemistry of Interfaces* (John Wiley I & Sons, Ltd, 2003).
30. G. E. Jellison, "3 - Data analysis for spectroscopic ellipsometry," in *Handbook of Ellipsometry*, H. G. Tompkins and E. A. Irene, eds. (William Andrew Publishing, Norwich, NY, 2005), pp. 237–296.
31. D. A. G. Bruggeman, "Berechnung verschiedener physikalischer konstanten von heterogenen substanzen. i. dielektrizitätskonstanten und leitfähigkeiten der mischkörper aus isotropen substanzen," Ann. Phys. **416**(8), 665–679 (1935).
32. W.-Y. Ching, Y.-N. Xu, and K. W. Wong, "Ground-state and optical properties of Cu_2O and C_uO crystals," Phys. Rev. B **40**(11), 7684–7695 (1989).
33. E. D. Palik, *Handbook of Optical Constants of Solids* (Academic Press, 1985).
34. M. Makry and L. Klinkenbusch, "Using the Kramers-Kronig transforms to retrieve the conductivity from the effective complex permittivity," Adv. Radio Sci. **16**, 23–28 (2018).
35. M. I. Alonso and M. Garriga, *Optical Properties of Semiconductors* (Springer International Publishing, 2018), pp. 89–113.
36. M. Di, E. Bersch, A. C. Diebold, S. Consiglio, R. D. Clark, G. J. Leusink, and T. Kaack, "Comparison of methods to determine bandgaps of ultrathin HfO_2 films using spectroscopic ellipsometry," J. Vac. Sci. Technol., A **29**(4), 041001 (2011).
37. G. E. Jellison and F. A. Modine, "Parameterization of the optical functions of amorphous materials in the interband region," Appl. Phys. Lett. **69**(3), 371–373 (1996).
38. J. Tauc, R. Grigorovici, and A. Vancu, "Optical properties and electronic structure of amorphous germanium," Phys. Status Solidi B **15**(2), 627–637 (1966).
39. J. Navratil, P. Levinsky, J. Hejtmanek, M. Pashchenko, K. Knízek, L. Kubickova, T. Kmjec, and C. Drasar, "Peculiar magnetic and transport properties of $CuFeS_2$: Defects play a key role," J. Phys. Chem. C **124**(38), 20773–20783 (2020).
40. R. Ang, A. U. Khan, N. Tsujii, K. Takai, R. Nakamura, and T. Mori, "Thermoelectricity generation and electron–magnon scattering in a natural chalcopyrite mineral from a deep-sea hydrothermal vent," Angew. Chem., Int. Ed. **54**(44), 12909–12913 (2015).
41. N. Sato, P. S. Gan, N. Tsujii, and T. Mori, "Effect of microstructure on lattice thermal conductivity of thermoelectric chalcopyrite $CuFeS_2$: experimental and computational studies," Appl. Phys. Express **14**(8), 087002 (2021).
42. W. H. Koschel, F. Sorger, and J. Baars, "Optical phonons in i-iii-vi2 compounds," Journal de Physique Colloques **36**(C3), 177–181 (1975).
43. A. Huber, N. Ocelic, D. Kazantsev, and R. Hillenbrand, "Near-field imaging of mid-infrared surface phonon polariton propagation," Appl. Phys. Lett. **87**(8), 081103 (2005).
44. A. Sugathan, B. Bhattacharyya, V. V. R. Kishore, A. Kumar, G. P. Rajasekar, D. D. Sarma, and A. Pandey, "Why Does $CuFeS_2$ Resemble Gold?" J. Phys. Chem. Lett. **9**(4), 696–701 (2018).
45. C. F. Bohren and D. R. Huffman, *Absorption and Scattering of Light by Small Particles* (John Wiley & Sons, 2008).
46. P. N. Keating, "Relationship between the macroscopic and microscopic theory of crystal elasticity. I. primitive crystals," Phys. Rev. **152**(2), 774–779 (1966).
47. H. Lysne, T. Brakstad, M. Kildemo, and T. Reenaas, "Improved methods for design of PLD and combinatorial PLD films," J. Appl. Phys. **132**(12), 125301 (2022).